



Strain regulation of bond length in single Ru sites via curving support surface for enhanced hydrogen evolution reaction

Yan Liu^a, Liwen Xing^{a,*}, Yaqi Liu^a, Dianxing Lian^a, Mohaoyang Chen^a, Weiwei Zhang^a,
Ke Wu^a, Hongdan Zhu^{b,*}, Zhiyi Sun^c, Wenxing Chen^c, Peng Wu^d, Dingsheng Wang^e,
Yongjun Ji^{a,*}

^a School of Light Industry Science and Engineering, Beijing Technology and Business University, Beijing 100048, China

^b State Key Laboratory and Institute of Elemento-Organic Chemistry, College of Chemistry, Nankai University, Tianjin 300071, China

^c Energy & Catalysis Center, School of Materials Science and Engineering, Beijing Institute of Technology, Beijing 100081, China

^d Shanghai Key Laboratory of Green Chemistry and Chemical Processes, Department of Chemistry, East China Normal University, Shanghai 200062, China

^e Department of Chemistry, Tsinghua University, Beijing 100084, China

ARTICLE INFO

Keywords:

Curved support

Strain

Ruthenium single atom

Bond length

Hydrogen evolution reaction

ABSTRACT

The intrinsic activity of single-atom catalysts is influenced by the local electronic structures of metal centers, with existing modulation strategies limited to adjacent atomic coordination. However, the impacts of support surface geometry on local bonding environment, and thus electronic structures of single-atom centers have rarely been known. Here, we prepared highly curved B,N co-doped carbon-supported ruthenium catalyst with an ultra-low Ru loading of 0.4 wt%, which exhibited an ultrahigh turnover frequency (TOF) of 10 H₂ s⁻¹ (38 times that of Pt/C) and superior stability in alkaline hydrogen evolution reaction (HER). We found that curving support surface induced the strain, resulting in 1.5% compressed Ru-N and 4% stretched Ru-B bonds, leading to the accumulation of positive charge and quenching of spin polarization at Ru sites, thereby achieving the optimal binding of H* and enhanced performance for HER. This work highlights the significant support effects upon the structural design of active sites.

1. Introduction

Sustainable hydrogen harvesting from water electrolysis, especially powered by renewable and intermittent energy, can offer a promising solution to the ultimate goal of carbon neutrality [1,2]. At present, due to a lack of effective electrode catalysts in commercial acidic electrolytes, alkaline electrolysis cells are technically more suitable for producing electrocatalytic hydrogen [3–5]. Consequently, the development of cost-effective electrocatalysts in alkaline media holds the key to the practical application of hydrogen evolution reaction (HER). To this end, great efforts have been devoted to developing high active and durable alternatives such as modified RuO₂ [6], Ru SACs [7], and Ru coordinated with other metals [8] to noble metal-based electrocatalysts like commercial Pt/C (20 or 40 wt%). In terms of catalytic activity, an efficient HER electrocatalyst must enable neither too strong nor too weak adsorption of activated H* intermediate, based on the classic Sabatier principle [9,10]. In this sense, various strategies have been devised to

attempt to adjust the adsorption strength of active components and H*, such as defect engineering [11,12], ligand engineering [13–15], heterostructures [16–19], and strain engineering [20,21], but how to achieve the optimal binding of H* over a catalyst still remains very challenging.

Metal single-atom catalysts stood out among the family of diverse HER electrocatalysts, owing to the maximum atomic utilization efficiency, high reactivity and structural stability [22–25]. Actually, the intrinsic activity of a single-atom catalyst is largely dictated by electronic structures of isolated metal centers over the support matrix [26–28]. Accordingly, considerable efforts focused on the electronic structure modulation of single-atom metal centers and thus desired catalytic performance, primarily by virtue of tailoring local coordination environment of single-atom metal centers [29–31]. Specifically, engineering the central metals [32], the coordination numbers [33], coordinated heteroatoms [34–36] and spin configuration [37,38] have been explored [39]. Especially, the construction of asymmetric heteroatom-coordinated single-atom metal centers was recently utilized

* Corresponding authors.

E-mail addresses: xingliwen@btbu.edu.cn (L. Xing), 1120180273@mail.nankai.edu.cn (H. Zhu), yjji@btbu.edu.cn (Y. Ji).

<https://doi.org/10.1016/j.apcatb.2024.124088>

Received 16 February 2024; Received in revised form 12 April 2024; Accepted 16 April 2024

Available online 17 April 2024

0926-3373/© 2024 Elsevier B.V. All rights reserved.

for subtly reshaping charge distribution of central metal, resulting in sensitive modulation of adsorption-desorption behaviors for key reaction intermediates and thus precise control of the catalytic activity [40–42]. However, there were still plenty of room to exploit the electronic structure sensitivity of single-atom metal center to regulate the associated catalytic performance, by other means such as the geometric variations of the support surface [43]. It is envisaged that with respect to asymmetric heteroatom-coordinated single-atom metal catalysts, curving or sharpening the support surface could introduce strain effect [44–46] and probably changes the coordination bond environment between single-atom metal center and surrounding coordinated heteroatoms such as bond length, thereby providing new opportunities for the regulation of electronic structure and adsorption strength for key reaction intermediates and thus the enhanced catalytic performance. Up to now, related reports are very rare [47] but highly desired [48].

In this work, we synthesized highly curved and tubular B,N co-doped carbon-supported ruthenium (Ru) catalyst with an ultra-low Ru loading of 0.4 wt%, revealing a Pt-like apparent activity and ultrahigh intrinsic activity toward alkaline HER. The selection of Ru as the active component is mainly because of its lower cost and similar binding strength with hydrogen compared to Pt. Particularly, the measured turnover frequency (TOF) value reached $10 \text{ H}_2 \text{ s}^{-1}$ at the overpotential of 100 mV, much higher than that of the counterpart without surface curvature and reported Ru-based catalysts and even 38 times that of commercial Pt/C. The combination of structural characterizations and theoretical calculations demonstrated that the introduction of support surface curvature can generate strain effect on the RuN_2B_1 sites, and elongate the bond length between single-atom Ru center and neighboring coordinated heteroatom B while shorten the bond length between single-atom Ru center and neighboring coordinated heteroatom N, leading to more positive charge and the quenching of spin polarization around the Ru center and thus the optimal H^* binding strength. This work presents the significant role of support surface curvature in controlling electronic structure of active sites and the catalytic performance.

2. Experimental section

2.1. Chemicals

Urea ($\text{CH}_4\text{N}_2\text{O}$, 99%), Ruthenium(III) chloride hydrate ($\text{RuCl}_3 \cdot x\text{H}_2\text{O}$), Ethylene glycol (In the text was named as PEG, $\text{HO}(\text{CH}_2\text{CH}_2\text{O})_n\text{H}$, molecular weight (MW) = 2000 and 8000), Potassium chloride (KCl, 99.5%), Potassium hydroxide (KOH, 99.99%) were purchased from Macklin Inc (China). Potassium ferricyanide ($\text{K}_2\text{FeC}_6\text{N}_6$, $\geq 99.5\%$), Potassium ferrocyanide trihydrate ($\text{K}_4\text{FeC}_6\text{N}_6 \cdot 3\text{H}_2\text{O}$, 99.0%) were purchased from Aladdin Industrial Co. Ltd., China. Boric acid (H_3BO_3 , $\geq 99.5\%$) were purchased from FuChen Chemical Co. Ltd., China. Ethyl alcohol ($\text{C}_2\text{H}_6\text{O}$, 99.7%) were purchased from Mreda Co. Ltd., China. Nafion aqueous solution (5.0 wt%) were purchased from Chemours Co. Ltd., China. Platinum on carbon (Pt/C, 20%) were purchased from HESEN Co. Ltd., China. All the chemicals were used as received without further purification. N_2 used in the experiment were purchased from White Martins, Co. Ltd., China.

2.2. Preparation of catalyst

Synthesis of RuBNC_x ($x = 1000, 1500, 2000, 4000$ and 8000 , which represent the molecular weight of PEG). The RuBNC_x were typically prepared via an integrated wet chemistry-pyrolysis strategy. Firstly, urea (5.5 g), boric acid (0.15 g), PEG2000 (0.5 g) and ruthenium trichloride (8.29 mg) was completely dissolved in ultrapure water (10–15 mL) under continuous magnetic stirring. The mixture solution was then rapidly cooled to ice upon the liquid nitrogen pouring, followed by the lyophilization. The obtained powder was heated to 1173 K at a ramping rate of 5 K min^{-1} and annealed for 2 h in a nitrogen flow (50 mL min^{-1}). After naturally cooling down to room temperature, the

final product was denoted as RuBNC2000 for further use. The control sample without any metal contents was also synthesized and marked as BNC2000 . Likewise, the corresponding products were named RuBNC1000 , RuBNC1500 , RuBNC4000 , and RuBNC8000 , when keeping other synthetic conditions only varying the average molecular weight of PEG to 1000, 1500, 4000, and 8000. Moreover, RuBC2000 , RuNC2000 , and RuBN2000 were also prepared using the same procedure with RuBNC2000 , albeit without the inclusion of urea, boric acid, and PEG2000. Also, samples of RuBNC2000 with different amount of ruthenium trichloride (0.02 mmol, 0.06 mmol, and 0.08 mol) were obtained and labeled as 0.02RuBNC2000 , 0.06RuBNC2000 , and 0.08RuBNC2000 .

2.3. Physical characterization

The scanning electron microscope (SEM, SU8010, Hitachi, Japan) and transmission electron microscope (TEM, JEM-2100 F, JEOL, Japan) were used to observe morphology and microstructure of as-prepared samples. The high-angle annular dark-field scanning transmission electron microscope (HAADF-STEM) equipped with energy dispersive X-ray spectrometer (EDS) were carried out using a Cs-corrected microscope (JEM-ARM300F, JEOL, Japan) operated at 200 kV. The structure and phase of the products were characterized by X-ray powder diffraction (XRD, D2PHASER, Bruker) with $\text{Cu K}\alpha$ radiation ($\lambda = 1.5418 \text{ \AA}$) at 30 kV, then comparing with the standard cards of the joint committee on powder diffraction standards (JCPDS). The concentration of Ru in various samples was measured on the inductively coupled plasma optical emission spectrometer (ICP-OES). The Raman spectra was recorded on a Raman microscope (XPLORA PLUS, HORIBA, Japan) with an excitation laser wavelength of 532 nm. Nitrogen adsorption/desorption isotherms were measured at 77 K using an automated surface area and pore size analyzer (v-sorb 2800, Gold APP Instruments, China). The specific surface area was determined by the Brunauer-Emmett-Teller (BET) equation. The pore size distribution was obtained from the desorption branch of isotherms by using the Barrett-Joyner-Halenda (BJH) model. The surface chemical composition of samples was measured by an X-ray photoelectron spectroscopy (XPS, ESCALAB 250xi, Thermo Fisher Scientific, America) with a non-monochromatized $\text{Al K}\alpha$ X-ray source (1486.6 eV). X-ray absorption fine structure (XAFS) spectra data (Ru L3-edge) were collected at station 1W1B in the Beijing Synchrotron Radiation Facility (BSRF), which operates at 2.5 GeV with a maximum current of 250 mA. The XAFS spectra of Ru foil and bulk RuO_2 references were collected in transmission mode, RuBNC2000 and RuBNC8000 in fluorescence mode. All samples were pelletized as disks of 13 mm diameter with 1 mm thickness using graphite powder as a binder. The acquired extended X-ray absorption fine structure (EXAFS) and X-ray absorption near-edge structure (XANES) data were processed according to the standard procedures using the Athena and Artemis implemented in the IFEFFIT software packages as follows:

The EXAFS spectra were obtained by subtracting the post-edge background from the overall absorption and then normalizing with respect to the edge-jump step. Subsequently, the $\chi(k)$ data were Fourier transformed to real (R) space using hanging windows ($\text{dk}=1.0 \text{ \AA}^{-1}$) to separate the EXAFS contributions from different coordination shells. Least-squares curve parameter fitting was performed using the ARTEMIS module of IFEFFIT software packages to obtain the quantitative structural parameters around central atoms. The following EXAFS equation was used:

$$\chi(k) = \sum_j \frac{N_j S_0^2 F_j(k)}{k R_j^2} \exp[-2k^2 \sigma_j^2] \exp\left[\frac{-2R_j}{\lambda(k)}\right] \sin[2kR_j + \Phi_j(k)]$$

S_0^2 is the amplitude reduction factor, $F_j(k)$ is the effective curved-wave backscattering amplitude, N_j is the number of neighbors in the j^{th} atomic shell, R_j is the distance between the X-ray absorbing central atom and the atoms in the j^{th} atomic shell (back scatterer), λ is the mean free path in \AA ,

$\Phi_j(k)$ is the phase shift (including the phase shift for each shell and the total central atom phase shift), σ_j^2 is the Debye-Waller parameter of the j^{th} atomic shell (variation of distances around the average R_j). The functions $F_j(k)$, λ and $\Phi_j(k)$ were calculated with the ab initio code FEFF8.2. The additional details for EXAFS simulations are given below. The coordination numbers of model samples were fixed as the nominal values. The obtained S_0^2 was fixed in the subsequent fitting. While the internal atomic distances R , DebyeWaller factor σ^2 and the edge-energy shift ΔE_0 were allowed to run freely.

2.4. Electrochemical tests

The electrochemical performance of as-prepared samples was performed in a conventional three-electrode cell with an electrochemical workstation (CHI 660E) at room temperature. The different samples modified glassy carbon electrode acted as working electrode, Ag/AgCl (saturated KCl) as reference electrode and a graphite rod (99.999%) as counter electrode. Typically, a certain amount of catalyst samples and volume of Nafion solution (5 wt%) were added and ultrasonically dispersed in water/isopropanol (1:1, v/v) to form a homogeneous ink. The obtained concentration of catalyst and Nafion were kept 5 mg mL⁻¹ and 0.5 wt%, respectively. Then, 5 μ L of catalyst ink was cast onto a clean glassy carbon electrode (diameter 3 mm, geometric area 0.07 cm²), which was then dried under an infra-red lamp for further use. Linear sweep voltammetry (LSV) was conducted in N₂ saturated KOH solution (1.0 M) with a scan rate of 5 mV s⁻¹. All the polarization curves were automatically IR-corrected. All the potentials were calibrated to a reversible hydrogen electrode (RHE) according to the Nernst's equation:

$$E(\text{vs. RHE}) = E(\text{vs. Ag/AgCl}) + 0.197 + 0.0591pH \quad (1)$$

The Tafel curves were extracted from the corresponding linear regions of overpotential against the logarithm of current density, based on Tafel equation:

$$\eta = b \log|j| + a \quad (2)$$

Where η , j , b and a were overpotential, current density, Tafel slope and intercept of longitudinal axis, respectively.

Turnover frequency (TOF), which is always defined as the number of hydrogen molecules generated per second per active site, can be calculated based on the following equation:

$$TOF = \frac{I}{2nF} \quad (3)$$

Where I (A) was the value of catalytic current in LSV measurement, n (mol) was the number of the catalytically active sites, F (96500 C mol⁻¹) was the Faraday's constant and the factor 1/2 meant that two electrons were required to form one hydrogen molecule. Note: we assumed that all the metallic contents participated in the electrochemical HER process for various metal-containing electrocatalysts.

Current-time (I-t) curve was recorded to investigate the stability of electrocatalysts at a fixed overpotential without IR-compensation to drive 10 mA cm⁻² of current density.

Cyclic voltammetry (CV) was performed in the non-Faradaic region from 0.15 to 0.25 V (vs. RHE) at varying scan rates (10, 30, 50, 70 and 90 mV s⁻¹) to investigate the electrochemically active surface area (ECSA). By plotting the difference of current density between the anodic and cathodic scans at 0.2 V (vs. RHE) against the scan rate, a linear trend was observed. The slope of the fitted line was just equal to twice the double layer capacitance (C_{dl}) of electrode. Thus, the ECSA (cm²) can be estimated as follows:

$$ECSA = \frac{C_{dl}}{C_s} A_{geo} \quad (4)$$

Where C_{dl} (mF cm⁻²) was the electrochemical double layer capacitance

of modified electrode, C_s (0.04 mF cm⁻²) and A_{geo} (0.07 cm²) were the specific capacitance and geometric area of a flat electrode surface, respectively.

2.5. DFT calculation methods

Spin polarized density functional theory (DFT) calculations were performed by using the Vienna Ab-initio Simulation package (VASP) [49]. The plane wave basis set was used with 500 eV energy cutoff and the projector augmented wave (PAW) was used [50]. Revised Perdew-Burke-Ernzerhof (RPBE[51] functional was used as exchange-correlation functional, while van der Waals correction was included. The H adsorption energy is calculated using following equation:

$$E_{ads} = E_{\text{surface+H}} - E_{\text{surface}} - 1/2E_{H_2} \quad (5)$$

And the H adsorption free energy is:

$$\Delta G_{H^*} = E_{ads} + \Delta ZPE - T\Delta S \quad (6)$$

where $E_{\text{surface+H}}$, E_{surface} , E_{H_2} are energy of hydrogenated surface slab, pure surface slab, and hydrogen molecule. The T and S are absolute temperature, and entropy change of hydrogen adsorption at 298 K, respectively. The $\Delta ZPE - T\Delta S$ value is 0.24 eV for H on Ru [52].

3. Results and discussion

3.1. Synthesis and structural properties

As schematically illustrated in Fig. 1a, the B and N co-doped carbon (BNC) supported Ru sites were typically synthesized via the freeze drying followed by a controlled pyrolysis. Since the other synthetic conditions kept the same, the remarkable surface curvature of tubular RuBNC2000 relative to lamellar RuBNC8000 might be attributed to the different molecular weight of PEG added during the synthesis. In the absence of PEG (RuBN), a disordered morphology was observed (Figure S1). Therefore, PEG was supposed to act as the structure-directing agent to induce curvature difference in the final products. The structural influence of PEG has been elucidated in prior research [53]. Specifically, the use of PEG with a molecular weight of 8000 leads to the generation of a large rectangular carbon plate. This structure impedes the rolling of the carbon plate and, consequently, the formation of a tubular configuration. Conversely, a decrease in the molecular weight of PEG induces the folding of the structure, resulting in the formation of a tubular structure. Notably, the use of the synthesized carbon nanotube as a support was quite different from the previously reported situation in which commercially available carbon nanotubes were directly employed as the substrate for Ru species loading [54]. Because the growth of carbon nanotubes was frequently catalyzed by transition metals (Fe, Co, Ni etc.) that easily remained inside the tubular cavity and unable to be completely removed, and thus the presence of metal impurities was likely to interfere the identification of catalytically active sites to a certain degree.

As shown in Fig. 1b, RuBNC2000 exhibited a well-defined hollow and tubular shape with a large aspect ratio. Its average wall thickness and external diameter were around 20 nm and 100 nm (Figure S2 and S3), respectively. Typical selected area electron diffraction (SAED) pattern showed quite dispersive feature in Figure S4, indicative of the poor crystalline nature of RuBNC2000. When enlarged as marked in Fig. 1c, homogeneous distribution of ultrafine nanoparticles was observed with the average size of 2 nm (Fig. 1d and S5). The lattice fringe spacing of these nanoparticles was measured to be 0.210 nm, basically consistent with that of standard Ru(100) facets (0.213 nm) (Figure S6), indicating the presence of Ru nanoparticles. When further zoomed on the edge of the tubular support under the aberration-corrected HAADF-STEM, there appeared a few bright dots, distributed

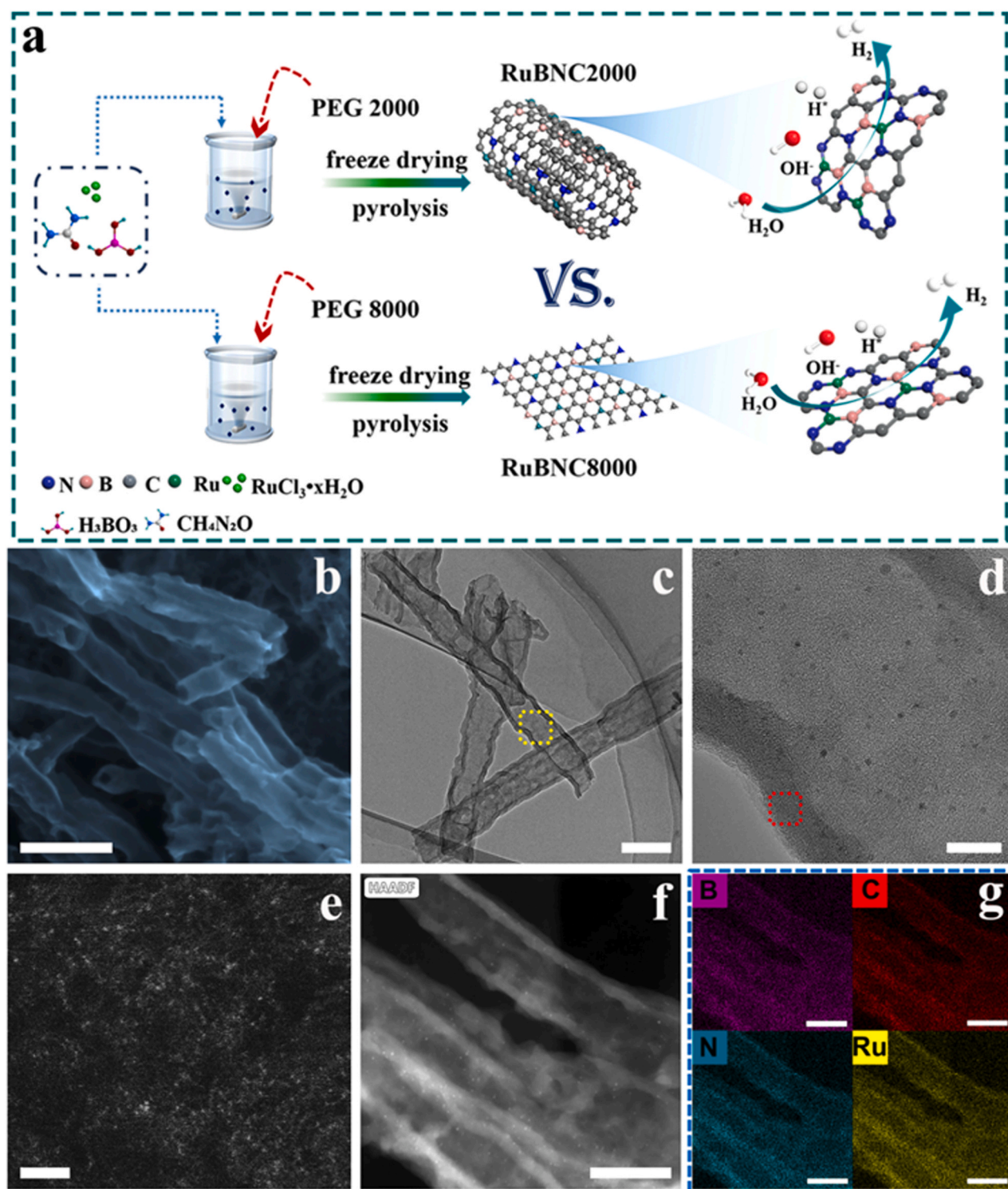


Fig. 1. (a) Schematic illustration of the synthesis of RuBNC2000 and RuBNC8000. (b) SEM, (c) TEM, (d) HRTEM and (e) atomic-resolution HAADF-STEM images of RuBNC2000. (f) High-resolution HAADF-STEM image of RuBNC2000 and (g) the corresponding EDS elemental mapping images of B, N, C and Ru. Scale bar: (b) 400 nm; (c) 200 nm; (d) 20 nm; (e) 2 nm; (f, g) 100 nm.

randomly and discretely as revealed in Fig. 1e and S7. The result confirmed the existence of atomically dispersed Ru sites over the support, based on the distinct Z contrast between Ru and light elements of the support. The HAADF-STEM image (Fig. 1f) and corresponding EDS elemental mapping (Fig. 1g and S8) results revealed the uniform distribution of B, C, N and Ru, verifying the formation of B and N co-doped carbon support as well. Except the distinct support surface curvature,

other similar situations including layer thickness, poor crystalline nature, the coexistence of Ru single atoms and ultrafine nanoparticles, and uniform element distribution, were also observed for RuBNC8000 (Figure S9). RuBNC4000 had a smaller curvature, between RuBNC2000 and RuBNC8000 (Figure S10 and S11). For BNC2000 in the absence of Ru contents, highly curved and tubular morphology was also observed, similar with that of RuBNC2000 (Figure S12).

As shown in Fig. 2a, all the XRD patterns manifested two broad peaks centered around 23° and 42° , which could be assigned to the characteristic diffraction from (002) and (101) planes of quasi-graphitic carbon [55], respectively. For both RuBNC2000 and RuBNC8000, no diffraction peaks corresponding to metallic Ru (standard card JCPDS No. 06-0663) were observed, indicating that Ru species was highly dispersed within the samples. Altogether, the XRD and electron microscopy results jointly confirmed that the BNC-supported Ru species was highly dispersed in the form of both single atoms and small-sized nanoparticles. To further study structural features of BNC supports, Raman spectra of all the samples (Fig. 2b) were analyzed by fitting the profile with the four characteristic bands: D1 (1228 cm^{-1}), D (1350 cm^{-1}), D3 (1517 cm^{-1}), and G (1588 cm^{-1}) [56]. Generally, the intensity ratio of D to G band (I_D/I_G) can quantify the extent of defects or graphitization in carbon materials. Namely, the larger I_D/I_G , the more defective structures present. As shown in Table S1, the calculated values of I_D/I_G were 1.15, 1.12 and 1.79 for RuBNC2000, RuBNC8000 and BNC2000, respectively. Compared with BNC2000, the pronounced decreased I_D/I_G and thus less defects can be observed within the two Ru-containing counterparts, which was likely attributed to the doping of Ru into carbon lattice vacancy [57]. Notably, almost the near I_D/I_G ratios signified the similar degree of carbon defects or graphitization for the two Ru-containing samples. Moreover, the similar Ru content for RuBNC2000 and RuBNC8000 was demonstrated by inductively coupled plasma optical emission spectrometer.

XPS was performed to examine the surface elemental composition and chemical contents of B, C, N, O and Ru for both RuBNC2000 and RuBNC8000 (Figure S13 and Table S3). state of different samples. There were similar elemental To figure out the possible bonding configurations, the corresponding high-resolution XPS spectra of B 1s, C 1s, N 1s, O 1s and Ru 3p were further deconvoluted into a few sub-peaks. As shown in Fig. 2c, the XPS spectra of B 1s can be well fitted into four types of B moieties ascribed to the B-C (193.23 eV), B-O (192.43 eV), B-N (191.59 eV), and Ru-B_x (190.59 eV), respectively [55]. In the case of N 1s (Fig. 2d), various N moieties such as N-B (398.08 eV), pyridinic (398.55 eV), pyrrolic (399.99 eV), graphitic (401.39 eV), and Ru-N_x (398.79 eV) can be well fitted. Note that the peak of Ru-N in the N 1s spectrum of RuBNC2000 exhibited a slight shift towards lower binding energy, likely influenced by curvature, which aligns with previous studies indicating that the binding energy of N 1s in B-N structures is slightly lower than 398 eV in carbon nanotubes with curvature [58,59], whereas on flat carbon substrates, the binding energy of N 1s in B-N structures tends to be slightly higher than 398 eV [60,61]. In addition, the C 1s spectra (Figure S14a) of the two Ru-based samples could be deconvoluted into four peaks at 284.36 eV (C=C), 285.16 eV (C-C/C-N), 285.96 eV (C=O), and 289.14 eV (O-C=O) [62]. The fitting of O 1s spectra (Figure S14b) excluded the presence of Ru-O species, which might be ascribed to the physicochemical adsorption of oxygenated species [63]. The Ru 3p XPS spectra (Figure S15) of RuBNC2000 and RuBNC8000 showed the binding energies of Ru $3p_{1/2}$ and Ru $3p_{3/2}$

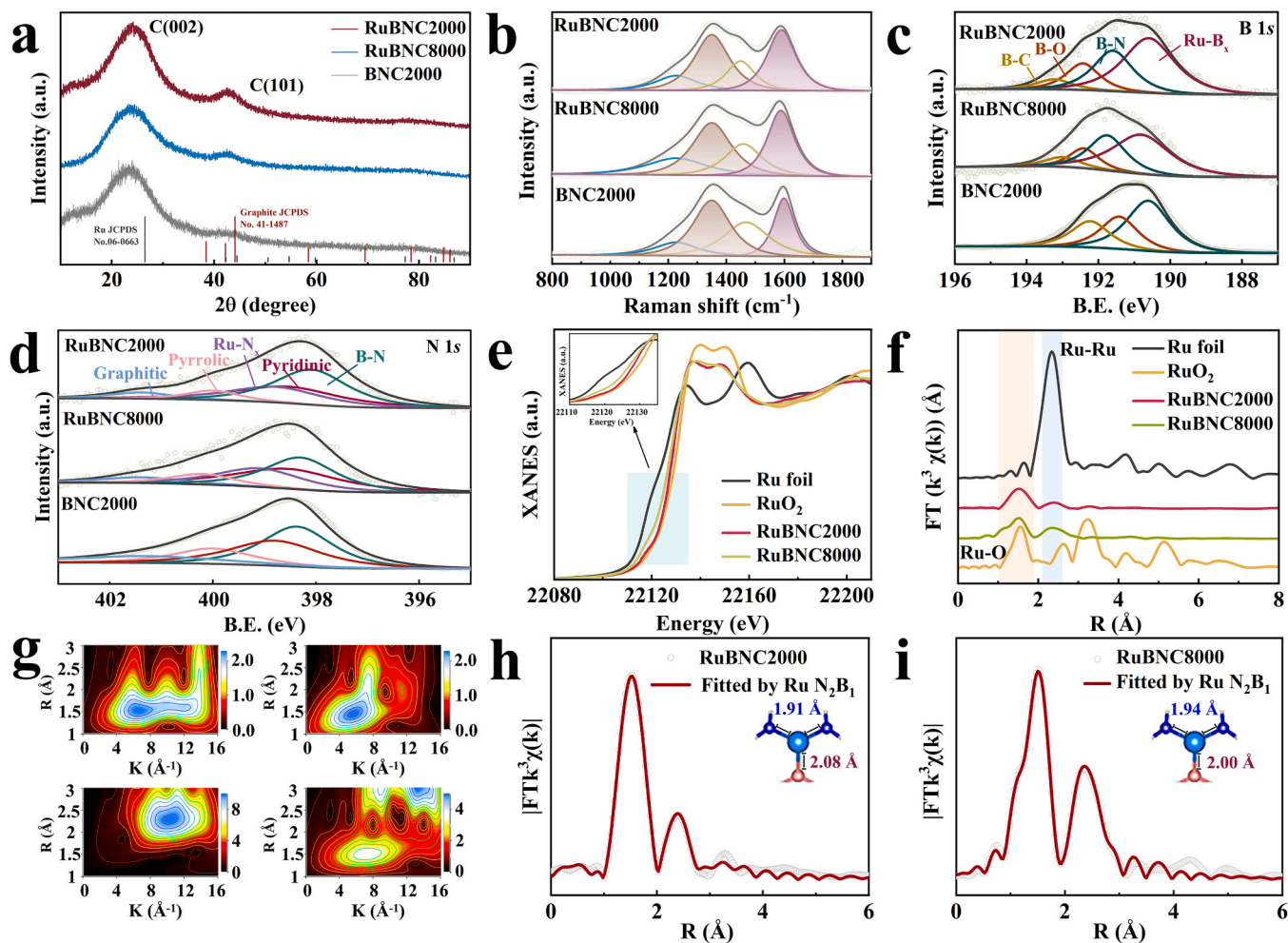


Fig. 2. (a) XRD patterns, (b) Raman spectra, (c) B 1s XPS spectra, and (d) N 1s XPS spectra of RuBNC2000, RuBNC8000 and BNC. (e) Ru K-edge XANES spectra and (f) R-space EXAFS curves of RuBNC2000, RuBNC8000, RuO₂ and Ru foil. (g) The WT-EXAFS plots of RuBNC2000, RuBNC8000, RuO₂, and Ru foil. Simulated structures and EXAFS fitting in R space for (h) RuBNC2000 and (i) RuBNC8000. Images h and i: Ru (blue), N (dark blue), B (pink).

centered at 487.1 eV and 464.9 eV for Ru^{2+} (SA-Ru bonded with N or B) as well as $\text{Ru } 3p_{1/2}$ and $\text{Ru } 3p_{3/2}$ at 484.3 eV and 462.1 eV for Ru^0 , with almost equal contents of Ru^0 and Ru^{2+} [58]. The slight positive shift of Ru 3p peak in RuBNC2000 compared with that in RuBNC8000 suggested the accumulation of more positive charge at the Ru sites of RuBNC2000 (Figure S15).

XANES and EXAFS spectra of Ru K-edge were further exploited to probe the accurate geometric/electronic structure of Ru species in our samples. As shown in Fig. 2e, the absorption edge of Ru between Ru foil and RuO_2 in our samples indicated that the average valence state of Ru species was situated between 0 and +4. Compared with that of RuBNC8000, there was more positive shift observed for RuBNC2000, suggesting the average Ru site with more positive charge, in line with the above XPS results (Figure S15). The result might be due to effect of local environmental strain of RuBNC2000 with support surface curvature. EXAFS analysis was performed to obtain bonding configuration of central Ru atoms in RuBNC2000 and RuBNC8000. As shown in Fig. 2f, the similar peaks assigned to the first coordination shell of isolated Ru sites can be observed at 1.534 and 1.503 Å for RuBNC2000 and RuBNC8000, respectively, ascribed to the Ru-N/C/B shell, indicating the possible presence of similar $\text{Ru-B}_x\text{C}_y\text{N}_z$ ($x+y+z \leq 4$, $x>0$) motif in both RuBNC2000 and RuBNC8000. In addition, similar small peak close to the Ru-Ru (2.33 Å) of Ru foil can be also observed in the two samples, further validating the formation of both Ru single atoms and nanoparticles in the two samples. Wavelet transform (WT) analysis also identified the presence of Ru-X ($X = \text{B}, \text{C}, \text{or N}$) moieties and Ru-Ru paths in RuBNC2000 and RuBNC8000 (Fig. 2g). The possible coordination configurations of the Ru center were further determined by the quantitative least-squares EXAFS curve-fitting analyses (Figs. 2h, 2i, S16 and S17). The best fitting results (Table S5) showed that the coordination numbers of Ru-N and Ru-B in RuBNC2000 or RuBNC8000 were around 2 and 1, respectively, suggesting that the atomically dispersed Ru sites in the two samples were most likely coordinated with one boron atom and two nitrogen atoms. Moreover, compared with that in RuBNC8000, the Ru-B bonds in RuBNC2000 was elongated by 4% while Ru-N bonds was

shortened by about 1.5%, suggesting generation of a certain level of tensile strain on Ru-B bonds and compressive strain on Ru-N bonds, resulted from the highly curved BNC support surface. Additionally, the formation energy among different coordination configurations via later theoretical calculation (see section of DFT calculations) further indicated that the RuN_2B_1 is indeed the most potential candidate moiety, consistent with the EXAFS analysis above.

3.2. Performance assessment

Alkaline HER performance of different catalysts was interrogated in detail in terms of catalytic activity and stability. For a given HER electrocatalyst, the apparent activity is most frequently evaluated by the overpotential required to deliver a current density of 10 mA cm^{-2} in linear sweep voltammetry (LSV). And it was more desired for the overpotential to afford smaller difference deviated from the theoretical value (0 mV vs. RHE). As shown in Fig. 3a and Figure S18, RuBNC2000 possessed high apparent HER activity with an overpotential of 41 mV at 10 mA cm^{-2} close to Pt/C benchmark (35 mV), much smaller than RuBNC8000 (167.6 mV), RuBNC4000 (102 mV), RuBNC1000 (207.6 mV), and RuBNC1500 (204 mV), implying the significance of curvature. Moreover, the overpotentials of RuBNC2000, RuBNC2000, and RuBNC2000 were measured to be 545 mV, 517 mV and 117.6 mV, respectively, which were also inferior to that of RuBNC2000, indicating that the coexistence of B, N and C is crucial (Figure S19). Further, for RuBNC2000, the results obtained from a lower scan rate (1 or 2 mV s^{-1}) exhibited no significant differences compared to a higher scan rate of 5 mV s^{-1} (Figure S20), suggesting the reliability of the data [64]. In strike contrast with RuBNC2000, BNC2000 had an overpotential of more than 900 mV due to the lack of catalytically active metal species, in turn indicating the decisive role of Ru species in the electrochemical HER activity of RuBNC2000. In brief, RuBNC2000 had Pt-like apparent HER activity in alkaline media. On the other hand, introducing either more or less the amounts of Ru source cannot further lower the overpotential (η_{10}) or Tafel slope of the resulting products (Figure S21a and S21b),

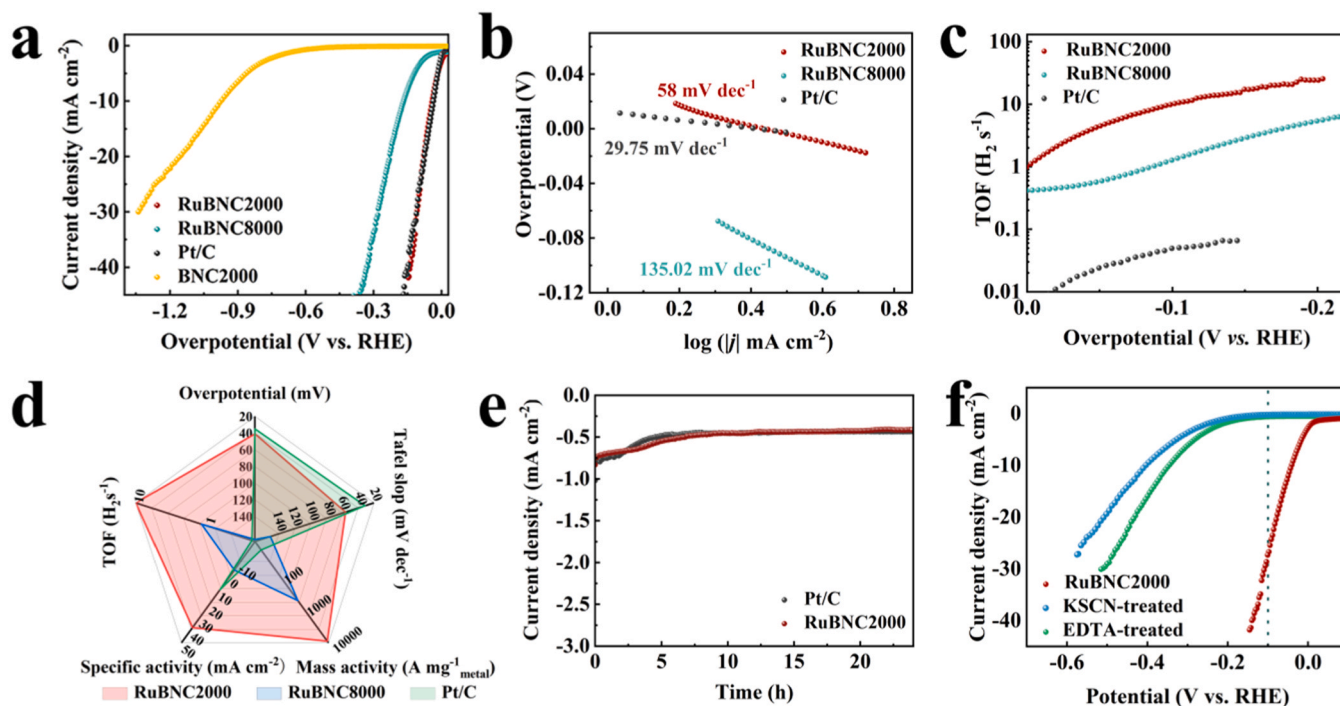


Fig. 3. (a) Polarization curves of different samples in 1.0 M KOH. (b) Tafel plots extracted from corresponding LSV curves. (c) The plot of TOF against the applied potential. (d) Integrated HER performance comparison of overpotential at 10 mA cm^{-2} , Tafel slope, and TOF, specific and mass activity at the overpotential of 100 mV for different catalysts. (e) Time-dependent current density curves of RuBNC2000 and Pt/C. (f) LSV curves of RuBNC2000 before and after the addition of 10 mM KSCN or EDTA into the electrolyte.

suggesting the optimized Ru contents within RuBNC2000. Likewise, the effect of higher or lower pyrolysis temperature on the catalytic activity was also assessed (Figure S22a and S22b), confirming the optimal temperature of 900 °C during the pyrolysis. Moreover, the Electrochemical Impedance Spectroscopy (EIS) test indicated that RuBNC2000 had a lower charge-transfer resistance than RuBNC8000 (Figure S23), aligning with the results obtained from the Tafel slope.

Tafel slope is closely linked with the reaction kinetics and possible reaction paths during the process of HER. Generally, the smaller its value, the faster HER kinetics present. As shown in Fig. 3b, Tafel slope of RuBNC2000 was calculated as 58 mV dec⁻¹, obviously smaller than that of RuBNC8000 (135.02 mV dec⁻¹), indicative of faster HER kinetics on RuBNC2000. According to theoretical deduction from Butler-Volmer equation (Figure S24), it can be concluded that the HER on RuBNC2000 proceeded via a mechanism of Heyrovsky reaction while RuBNC8000 tended to follow a Volmer reaction-controlled kinetics [2].

As is well-known in catalysis, turnover frequency (TOF) is usually regarded as the best figure of merit to reflect the intrinsic activity of a certain catalyst [65]. In electrochemical HER, TOF can be expressed as the function of applied potential, according to the Eq. 2 (the detail can be seen in Supporting Information) and recorded linear scanning voltammetry curve (Figure S25). Assumed that all the metallic content served as catalytically active sites of electrochemical HER, the TOF value of RuBNC2000 within the potential window was obviously higher than that of RuBNC8000 and Pt/C (Fig. 3c). For example, at the overpotential of 100 mV, the TOF value of RuBNC2000 (10 H₂ s⁻¹) was more than 8 folds that of RuBNC8000 (1.21 H₂ s⁻¹) and over 38 times that of Pt/C (0.26 H₂ s⁻¹). This suggested that RuBNC2000 owned the best intrinsic activity in our system. The turnover number (TON) is 161880, determined by the time (i-t method) required for hydrogen production during the electrolysis of 0.833 mol of H₂O, which is 16188 s. To alleviate the possible effect of metal loading and the exposure of active sites, both mass activity and specific activity were also evaluated by normalizing metal loading and electrochemically active surface area (ECSA), respectively. The results showed that RuBNC2000 also exhibited dramatically higher mass activity (Figure S26a) and specific activity (Figure S26b) than RuBNC8000 and Pt/C within the potential window. Given that the surface area or porosity of materials usually had significant influence upon the catalytic performance, we further normalized the catalytic current density by corresponding BET area and pore volume (Figure S27 and Table S6). The obtained results (Figure S28) indicated that both the specific surface area and pore volume were not the dominant structural factors determining the HER reactivity. All the activity parameters above, including overpotential at 10 mA cm⁻², Tafel slope, mass and specific activity and TOF at the overpotential of 100 mV, were vividly summarized in Fig. 3d. Moreover, the various activity parameters of RuBNC2000 were also comparable with and even better than those of diverse HER electrocatalysts in the literature, especially considering the very low Ru loading in our catalyst (Table S7). Notably, the TOF value of RuBNC2000 in our work is much higher than those of the previous reported Ru-based electrocatalysts (Figure S29).

The long-term durability is another important indicator of excellent HER performance. After 24 h of continuous electrolysis at original current density of 10 mA cm⁻², a performance decay of ca. 12.8% and 8.9% was observed for Pt/C and RuBNC2000, respectively, and the performance of RuBNC2000 tended to be stable after 6 h, as displayed in Fig. 3e. This result suggested that RuBNC2000 still possessed better stability than commercial Pt/C, which might result from the strong interactions between active Ru sites and the support. Note that the appearance of current fluctuation at I-t curves was supposed to result from the sequential accumulation and release of the generated H₂ bubbles on the electrode surface. Furthermore, the XRD patterns (Figure S30) and XPS spectra (Figure S31) indicated that there were no significant changes in the structure of RuBNC2000 after a 24 h stability test. Additionally, ICP analysis revealed no notable variations in the Ru content (Table S2).

Overall, the comprehensive HER performance analyses and comparisons had an implication for our RuBNC2000 being as one of the promising alternatives to the commercial Pt/C.

3.3. Activity origin

It has been generally accepted that the metal components within a catalyst are responsible for the overall catalytic activity. Due to the coexistence of both small-sized nanoparticles and single atoms in our system, poisoning experiments were designed to distinguish the individual contributions to the HER performance. Given that CN⁻ or SCN⁻ can strongly and indiscriminately adsorb onto Ru species in all their forms while ethylenediaminetetraacetic acid (EDTA) is merely inclined to coordinate with quasi-ionic single-atom sites [66], we deliberately introduced KSCN and EDTA dipotassium salt as poisoning agents into the electrolyte, respectively, to examine the changes of polarization curves. As seen, the original polarization curve showed different levels of negative shift and thus performance decay, indicating the active sites of RuBNC2000 was accordingly blocked to different degrees (Fig. 3f and Table S8). Specifically, the current density of RuBNC2000 at the overpotential of 100 mV dropped from 16.98 mA cm⁻² to 0.62 and 0.25 mA cm⁻², indicating that 96.4% and 98.6% of the accessibly active Ru sites were blocked after EDTA dipotassium salt and SCN⁻ treating, respectively [67,68]. In this case, single-atom Ru sites accounted for over 97.8% contributions of all the accessible Ru species to the catalytic current. Therefore, it can be concluded that single-atom Ru sites played absolutely a dominant role in the HER activity of RuBNC2000, while Ru nanoparticles made only minor contributions. Further, the comprehensive physicochemical characterizations above had confirmed the apparent structure similarity between RuBNC2000 and RuBNC8000, such as elemental composition, crystalline nature, and degree of defects or graphitization, which were supposed to have an equal effect on the intrinsic activity. Namely, those were not the dominant activity origins. Also, we had excluded the possible effects of structural aspects, including specific surface area and pore volume. Compared with that of RuBNC8000, the improved HER performance of RuBNC2000 can be attributed to the distinct support curvature difference. That was, the highly curved and tubular support of RuBNC2000 endowed the elongated coordination bonds of single-atom Ru center with B atom while shortened coordination bonds of single-atom Ru center with N atom, further leading to the concentration of positive charge and thus probably the optimal H⁺ binding strength.

3.4. DFT calculations

To further identify the possible chemical configurations of the Ru-N/C/B moieties, using DFT calculations, we examined and compared the hydrogen binding energy and the formation energy with a range of planar RuC_xN_yB_z (x+y+z ≤ 4, z>0) structures. Considering the formation energy of RuC_xN_yB_z and its catalytic activity in planar two-dimensional structures, data points of different stable structures are shown in Fig. 4a (see Figure S32 for details). An optimal configuration located in the bottom portion of the dark blue region that corresponds to a low formation energy and a |ΔG_{H*}| close to zero. Herein, RuN₂B₁ structure represents the optimal structure for HER, featuring a relatively low formation energy and a reasonable |ΔG_{H*}| (<0.4 eV) (Fig. 4a), consistent with the results of experimental characterization in Fig. 2h. Notably, whereas the RuC₁N₂B₁ moiety exhibits the lowest formation energy among possible structural configurations, with only 0.05 eV lower than that of RuN₂B₁, the relatively large |ΔG_{H*}| (0.73 eV) of the RuC₁N₂B₁ suggest that it is unlikely the catalytic active site (Table S9). Furthermore, to gain deeper insights into the structure-activity relationship of the curved RuN₂B₁ site, the RuN₂B₁ sites on curved surfaces (RuN₂B₁(8,8), RuN₂B₁(7,7), RuN₂B₁(6,6) and RuN₂B₁(5,5)) with different curvature were constructed in Fig. 4b. The surface curvature of different structures were calculated as 0.186, 0.214, 0.249 and

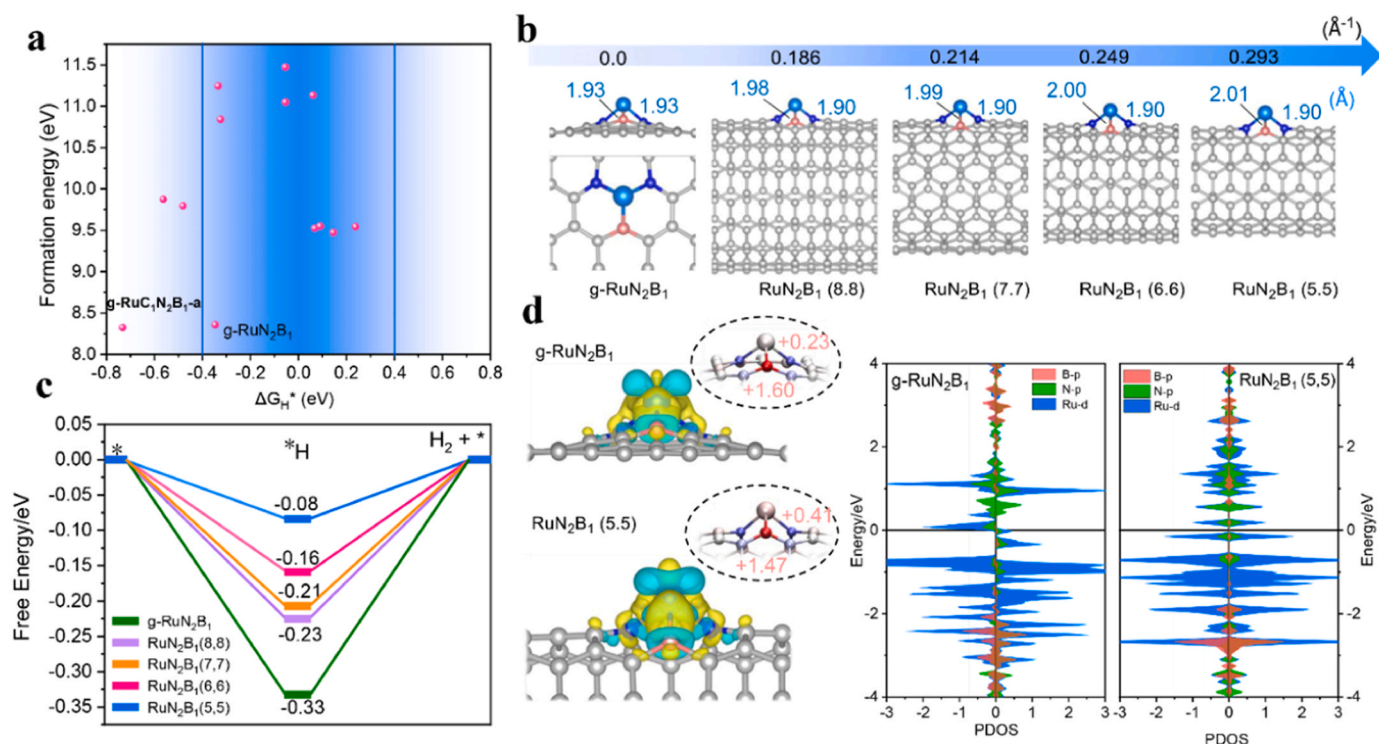


Fig. 4. (a) Energy diagram of different $\text{RuC}_x\text{N}_y\text{B}_z$ structures. (b) RuN_2B_1 sites on curved surfaces ($\text{RuN}_2\text{B}_1(8,8)$, $\text{RuN}_2\text{B}_1(7,7)$, $\text{RuN}_2\text{B}_1(6,6)$ and $\text{RuN}_2\text{B}_1(5,5)$) with different curvature, curvature of different structures was calculated via $1/R$, where R is the radius of the structure models (curvature in black and bond length in blue). (c) Hydrogen-adsorption free energies (ΔG_{H^*}) of RuN_2B_1 . (d) Differential charge density (yellow represents electron accumulation, and blue represents electron loss), Bader charge coloring map (red shows positive charge, and blue shows negative charge) and Partial Density of States (PDOS) diagram.

0.293 \AA^{-1} , respectively. Interestingly, as the curvature increases, the value of $|\Delta G_{H^*}|$ gradually close to zero (Fig. 4c). Compared with the calculated ΔG_{H^*} on planar $\text{g-RuN}_2\text{B}_1$ (-0.33 eV), the curved $\text{RuN}_2\text{B}_1(5,5)$ has a better ΔG_{H^*} value with -0.08 eV , close to zero, suggesting the curved $\text{RuN}_2\text{B}_1(5,5)$ is more favorable for the hydrogen evolution reaction (HER). Further electronic structure analysis showed that the enhanced HER was mainly derived from the strain regulation of single metal RuN_2B_1 sites. As shown in Fig. 4b, local strains of the RuN_2B_1 were induced as the curvature increases, resulting in 1.6% compressed Ru-N bonds and 4.1% stretched Ru-B bonds. In the micro-coordination structure of RuN_2B_1 (Figure S33), N atoms gained electrons while B atom lost electrons, resulting in the charge of $+0.23|e|$ on Ru. With the increase of curvature, the Ru-B bond length was significantly elongated in $\text{RuN}_2\text{B}_1(5,5)$, which weakens the covalent interaction between Ru and B. As a result, part of the electrons on the Ru feed back to the B atom, resulting in more aggregation of positive charges of $+0.41|e|$ on the Ru atoms (Fig. 4d), which is also consistent with the results of the above experimental characterization (Fig. 2e). The differential charge density and projected Partial Density of States (PDOS) indicated that partial electrons of Ru-d orbitals were transferred into B-p orbitals in the curved $\text{RuN}_2\text{B}_1(5,5)$ site, resulting in an upshifted d-orbital energy level and quenched spin polarization. In addition, the compressed Ru-N bond also results in more electrons transfer from Ru to N. The strain-regulated single atom Ru with high positive charge and quenched spin polarization lead to a weaker but more optimal H^* binding strength for hydrogen evolution. Therefore, the strain regulation of local chemical environment provided the proper models for exploring the influence of electronic properties of single atoms on electrochemical performance toward HER.

4. Conclusions

In summary, we successfully fabricate highly curved and tubular B, N

co-doped carbon support to load Ru sites with ultra-low Ru loading (0.4 wt%). This catalyst manifests not only an Pt-like apparent activity toward the HER in an alkaline solution, but also superior mass, specific, intrinsic activity and stability compared to commercial Pt/C. Especially, the TOF value at the overpotential of 100 mV reaches $10 \text{ H}_2 \text{ s}^{-1}$, much higher than that of the counterpart without surface curvature and most reported Ru-based catalysts and even 38 times that of commercial Pt/C. Combined structural characterization and theoretical calculation results demonstrate that introducing the surface curvature into the support can generate the strain and regulate local coordination bonds between single-atom Ru center and neighboring heteroatoms B and N, eliminate spin polarization and strengthen the positive charge of the Ru center, enable the optimized adsorption of H^* intermediate and thus the promotion in the catalytic efficiency. This work presents the straightforward and significant role of support surface geometry in directing electronic structure of active sites and thus the catalytic performance, providing new insights into the structure-performance correlations.

CRediT authorship contribution statement

Mohaoyang Chen: Investigation. **Weiwei Zhang:** Supervision, Resources. **Ke Wu:** Supervision, Resources. **Wenxing Chen:** Formal analysis. **Peng Wu:** Resources. **Hongdan Zhu:** Supervision, Resources. **Zhiyi Sun:** Formal analysis. **Yaqi Liu:** Investigation. **Dianxing Lian:** Investigation. **Dingsheng Wang:** Visualization, Supervision, Resources, Funding acquisition, Conceptualization. **Yan Liu:** Writing – original draft, Visualization, Validation, Investigation, Formal analysis, Data curation. **Yongjun Ji:** Writing – review & editing, Visualization, Supervision, Project administration, Methodology, Funding acquisition. **Liwen Xing:** Writing – review & editing, Visualization, Supervision, Resources, Methodology, Conceptualization.

Declaration of Competing Interest

The authors declare that they have no known competing financial interests or personal relationships that could have appeared to influence the work reported in this paper.

Data availability

Data will be made available on request.

Acknowledgements

We gratefully acknowledge the financial support from the Research Foundation for Youth Scholars of Beijing Technology and Business University (No. QNJJ2022-22 and QNJJ2022-23 from L.X. and K.W.); the National Natural Science Foundation of China (No. 22301012 from K.W.); the R&D Program of Beijing Municipal Education Commission (No. KM202310011005 from K.W.); the National Natural Science Foundation of China (No. 21978299 from Y.J.); the Research Foundation for Advanced Talents of Beijing Technology and Business University (No. 19008020159 from Y.J.).

Appendix A. Supporting information

Supplementary data associated with this article can be found in the online version at [doi:10.1016/j.apcatb.2024.124088](https://doi.org/10.1016/j.apcatb.2024.124088).

References

- J. Wan, Z. Zhao, H. Shang, B. Peng, W. Chen, J. Pei, L. Zheng, J. Dong, R. Cao, R. Sarangi, Z. Jiang, D. Zhou, Z. Zhuang, J. Zhang, D. Wang, Y. Li, In situ phosphatizing of triphenylphosphine encapsulated within metal-organic frameworks to design atomic $\text{Co}_1\text{-P}_1\text{N}_3$ interfacial structure for promoting catalytic performance, *J. Am. Chem. Soc.* 142 (2020) 8431–8439.
- Y. Liu, Q. Wang, J. Zhang, J. Ding, Y. Cheng, T. Wang, J. Li, F. Hu, H.B. Yang, B. Liu, Recent advances in carbon-supported noble-metal electrocatalysts for hydrogen evolution reaction: syntheses, structures, and properties, *Adv. Energy Mater.* 12 (2022) 2200928.
- Z. Li, W. Niu, Z. Yang, A. Kara, Q. Wang, M. Wang, M. Gu, Z. Feng, Y. Du, Y. Yang, Boosting alkaline hydrogen evolution: the dominating role of interior modification in surface electrocatalysis, *Energ. Environ. Sci.* 13 (2020) 3110–3118.
- Z.Y. Yu, Y. Duan, X.Y. Feng, X. Yu, M.R. Gao, S.H. Yu, Clean and affordable hydrogen fuel from alkaline water splitting: past, recent Progress, and future Prospects, *Adv. Mater.* 33 (2021) e2007100.
- X. Zheng, X. Shi, H. Ning, R. Yang, B. Lu, Q. Luo, S. Mao, L. Xi, Y. Wang, Tailoring a local acid-like microenvironment for efficient neutral hydrogen evolution, *Nat. Commun.* 14 (2023) 4209.
- Y. Li, W. Wang, M. Cheng, Y. Feng, X. Han, Q. Qian, Y. Zhu, G. Zhang, Arming Ru with oxygen vacancy enriched RuO_2 sub-nanometer skin activates superior bifunctionality for pH-universal overall water splitting, *Adv. Mater.* 35 (2023) 2206351.
- J.N. Tiwari, N.K. Dang, S. Sultan, P. Thangavel, H.Y. Jeong, K.S. Kim, Multi-heteroatom-doped carbon from waste-yeast biomass for sustained water splitting, *Nat. Sustain.* 3 (2020) 556–563.
- D. Wang, Q. Li, C. Han, Z. Xing, X. Yang, Single-atom ruthenium based catalyst for enhanced hydrogen evolution, *Appl. Catal. B-Environ.* 249 (2019) 91–97.
- Y. Zheng, Y. Jiao, M. Jaroniec, S.Z. Qiao, Advancing the electrochemistry of the hydrogen-evolution reaction through combining experiment and theory, *Angew. Chem. Int. Ed.* 54 (2015) 52–65.
- L. Wang, J. Wu, S. Wang, H. Liu, Y. Wang, D. Wang, The reformation of catalyst: from a trial-and-error synthesis to rational design, *Nano. Res.* (2023) 1–41.
- Q. Yang, T. Wang, Z. Zheng, B. Xing, C. Li, B. Li, Constructing interfacial active sites in $\text{Ru/g-C}_3\text{N}_4$ photocatalyst for boosting H_2 evolution coupled with selective benzyl-alcohol oxidation, *Appl. Catal. B-Environ.* 315 (2022) 121575.
- S. Chen, S. Wang, P. Hao, M. Li, Y. Zhang, J. Guo, W. Ding, M. Liu, J. Wang, X. Guo, N,O-C Nanocage-mediated high-efficient hydrogen evolution reaction on IrNi@N , O-C electrocatalyst, *Appl. Catal. B-Environ.* 304 (2022) 120996.
- J. Zhang, Y. Gu, Y. Lu, C. Zhu, G. Liu, C. Wang, D. Sun, Y. Tang, H. Sun, Each performs its own functions: nickel oxide supported ruthenium single-atoms and nanoclusters relay catalysis with multi-active sites for efficient alkaline hydrogen evolution reaction, *Appl. Catal. B-Environ.* 325 (2023) 122316.
- H. Jin, M. Ha, M.G. Kim, J.H. Lee, K.S. Kim, Engineering Pt coordination environment with atomically dispersed transition metal sites toward superior hydrogen evolution, *Adv. Energy Mater.* 13 (2023) 2204213.
- Y. Dai, H. Li, C. Wang, W. Xue, M. Zhang, D. Zhao, J. Xue, J. Li, L. Luo, C. Liu, X. Li, P. Cui, Q. Jiang, T. Zheng, S. Gu, Y. Zhang, J. Xiao, C. Xia, J. Zeng, Manipulating local coordination of copper single atom catalyst enables efficient CO_2 -to- CH_4 conversion, *Nat. Commun.* 14 (2023) 3382.
- F. Bi, Y. Su, Y. Zhang, M. Chen, J.A. Darr, X. Weng, Z. Wu, Vacancy-defect semiconductor quantum dots induced an S-scheme charge transfer pathway in OD/2D structures under visible-light irradiation, *Appl. Catal. B-Environ.* 306 (2022) 121109.
- Z. An, H. Xue, J. Sun, N. Guo, T. Song, J. Sun, Y. Hao, Q. Wang, Co-construction of sulfur vacancies and heterogeneous interface into $\text{Ni}_3\text{S}_2/\text{MoS}_2$ catalysts to achieve highly efficient overall water splitting, *Chin. J. Struc. Chem.* 41 (2022) 37–43.
- M. Wang, Y. Xu, C.-K. Peng, S.-Y. Chen, Y.-G. Lin, Z. Hu, L. Sun, S. Ding, C.-W. Pao, Q. Shao, X. Huang, Site-specified two-dimensional heterojunction of Pt nanoparticles/metal-organic frameworks for enhanced hydrogen evolution, *J. Am. Chem. Soc.* 143 (2021) 16512–16518.
- S. Qiao, Q. He, Q. Zhou, Y. Zhou, W. Xu, H. Shou, Y. Cao, S. Chen, X. Wu, L. Song, Interfacial electronic interaction enabling exposed Pt(110) facets with high specific activity in hydrogen evolution reaction, *Nano. Res.* 16 (2023) 174–180.
- Z. Jiang, S. Song, X. Zheng, X. Liang, Z. Li, H. Gu, Z. Li, Y. Wang, S. Liu, W. Chen, D. Wang, Y. Li, Lattice strain and schottky junction dual regulation boosts ultrafine ruthenium nanoparticles anchored on a N-modified carbon catalyst for H_2 production, *J. Am. Chem. Soc.* 144 (2022) 19619–19626.
- T. Zhang, Y. Liu, J. Yu, Q. Ye, L. Yang, Y. Li, H.J. Fan, Biaxially strained MoS_2 nanoshells with controllable layers boost alkaline hydrogen evolution, *Adv. Mater.* 34 (2022) 2202195.
- Y. Hu, T. Chao, Y. Li, P. Liu, T. Zhao, G. Yu, C. Chen, X. Liang, H. Jin, S. Niu, W. Chen, D. Wang, Y. Li, Cooperative Ni(Co)-Ru-P sites activate dehydrogenation for hydrazine oxidation assisting self-powered H_2 production, *Angew. Chem. Int. Ed.* 62 (2023) e202308800.
- J.N. Tiwari, S. Sultan, C.W. Myung, T. Yoon, N. Li, M. Ha, A.M. Harzandi, H. J. Park, D.Y. Kim, S.S. Chandrasekaran, W.G. Lee, V. Vij, H. Kang, T.J. Shin, H. S. Shin, G. Lee, Z. Lee, K.S. Kim, Multicomponent electrocatalyst with ultralow Pt loading and high hydrogen evolution activity, *Nat. Energy* 4 (2019), 249–249.
- H. Jin, S. Sultan, M. Ha, J.N. Tiwari, M.G. Kim, K.S. Kim, Simple and scalable mechanochemical synthesis of noble metal catalysts with single atoms toward highly efficient hydrogen evolution, *Adv. Funct. Mater.* 30 (2020) 2000531.
- L. Xing, Y. Jin, Y. Weng, R. Feng, Y. Ji, H. Gao, X. Chen, X. Zhang, D. Jia, G. Wang, Top-down synthetic strategies toward single atoms on the rise, *Matter* 5 (2022) 788–807.
- T. Gan, D. Wang, Atomically dispersed materials: ideal catalysts in atomic era, *Nano. Res.* 17 (2023) 18–38.
- G. Chen, R. Lu, C. Li, J. Yu, X. Li, L. Ni, Q. Zhang, G. Zhu, S. Liu, J. Zhang, U. I. Kramm, Y. Zhao, G. Wu, J. Xie, X. Feng, Hierarchically porous carbons with highly curved surfaces for hosting single metal FeN₄ sites as outstanding oxygen reduction catalysts, *Adv. Mater.* 35 (2023) 2300907.
- D. Wang, Q. Li, C. Han, Q. Lu, Z. Xing, X. Yang, Atomic and electronic modulation of self-supported nickel-vanadium layered double hydroxide to accelerate water splitting kinetics, *Nat. Commun.* 10 (2019) 3899.
- D. Wang, Y. Chen, L. Fan, T. Xiao, T. Meng, Z. Xing, X. Yang, Bulk and surface dual modification of nickel-cobalt spinel with ruthenium toward highly efficient overall water splitting, *Appl. Catal. B-Environ.* 305 (2022) 121081.
- Y. Ji, X. Chen, S. Liu, S. Song, W. Xu, R. Jiang, W. Chen, H. Li, T. Zhu, Z. Li, Z. Zhong, D. Wang, G. Xu, F. Su, Tailoring the electronic structure of single Ag atoms in Ag/WO_3 for efficient NO reduction by CO in the presence of O_2 , *ACS Catal.* 13 (2023) 1230–1239.
- P. Zhu, X. Xiong, D. Wang, Regulations of active moiety in single atom catalysts for electrochemical hydrogen evolution reaction, *Nano. Res.* 15 (2022) 5792–5815.
- H. Yang, D. Ma, Y. Li, Q. Zhao, F. Pan, S. Zheng, Z. Lou, Mo doped Ru-based cluster to promote alkaline hydrogen evolution with ultra-low Ru loading, *Chin. J. Struc. Chem.* 42 (2023).
- M. Kim, S.-h Kim, J. Park, S. Lee, I. Jang, S. Kim, C.Y. Lee, O.J. Kwon, H.C. Ham, J. T. Hupp, N. Jung, S.J. Yoo, D. Whang, Reconstructing oxygen-deficient zirconia with ruthenium catalyst on atomic-scale interfaces toward hydrogen production, *Adv. Funct. Mater.* 33 (2023) 2300673.
- X. Li, H. Rong, J. Zhang, D. Wang, Y. Li, Modulating the local coordination environment of single-atom catalysts for enhanced catalytic performance, *Nano. Res.* 13 (2020) 1842–1855.
- Y. Ji, S. Liu, S. Song, W. Xu, L. Li, Y. Zhang, W. Chen, H. Li, J. Jiang, T. Zhu, Z. Li, Z. Zhong, D. Wang, G. Xu, F. Su, Negatively charged single-atom Pt catalyst shows superior SO_2 tolerance in NO_x reduction by CO , *ACS Catal.* 13 (2023) 224–236.
- Z. Li, D. Wu, W. Gong, J. Li, S. Sang, H. Liu, R. Long, Y. Xiong, Highly efficient photocatalytic CO_2 methanation over Ru-doped TiO_2 with tunable oxygen vacancies, *Chin. J. Struc. Chem.* 41 (2022) 2212043–2212050.
- Y. Liu, J. Ding, F. Li, X. Su, Q. Zhang, G. Guan, F. Hu, J. Zhang, Q. Wang, Y. Jiang, B. Liu, H.B. Yang, Modulating hydrogen adsorption via charge transfer at the semiconductor-metal heterointerface for highly efficient hydrogen evolution catalysis, *Adv. Mater.* 35 (2023) 2207114.
- V. Giulimondi, S. Mitchell, J. Pérez-Ramírez, Challenges and opportunities in engineering the electronic structure of single-atom catalysts, *ACS Catal.* (2023) 2981–2997.
- D. Liu, Q. He, S. Ding, L. Song, Structural regulation and support coupling effect of single-atom catalysts for heterogeneous catalysis, *Adv. Energy Mater.* 10 (2020) 2001482.
- S. Wu, M. Chen, W. Wang, J. Zhou, X. Tang, D. Zhou, C. Liu, Molybdenum carbide nanoparticles assembling in diverse heteroatoms doped carbon matrix as efficient hydrogen evolution electrocatalysts in acidic and alkaline medium, *Carbon* 171 (2021) 385–394.

- [41] D. Liu, Y. Zhao, C. Wu, W. Xu, S. Xi, M. Chen, L. Yang, Y. Zhou, Q. He, X. Li, B. Ge, L. Song, J. Jiang, Q. Yan, Triggering electronic coupling between neighboring hetero-diatom metal sites promotes hydrogen evolution reaction kinetics, *Nano Energy* 98 (2022) 107296.
- [42] Y. Lei, Y. Wang, Y. Liu, C. Song, Q. Li, D. Wang, Y. Li, Designing atomic active centers for hydrogen evolution electrocatalysts, *Angew. Chem. Int. Ed.* 59 (2020) 20794–20812.
- [43] L. Xing, H. Gao, D. Jia, X. Chen, M. Han, J. Lv, A. Li, G. Wang, X. Shu, Cobalt-embedded few-layered carbon nanosheets toward enhanced hydrogen evolution: Rational design and insight into structure-performance correlation, *J. Energy Chem.* 58 (2021) 156–161.
- [44] L. Li, S. Liu, C. Zhan, Y. Wen, Z. Sun, J. Han, T.-S. Chan, Q. Zhang, Z. Hu, X. Huang, Surface and lattice engineered ruthenium superstructures towards high-performance bifunctional hydrogen catalysis, *Energ. Environ. Sci.* 16 (2023) 157–166.
- [45] J. Yang, Z. Wang, C.-X. Huang, Y. Zhang, Q. Zhang, C. Chen, J. Du, X. Zhou, Y. Zhang, H. Zhou, L. Wang, X. Zheng, L. Gu, L.-M. Yang, Y. Wu, Compressive strain modulation of single iron sites on helical carbon support boosts electrocatalytic oxygen reduction, *Angew. Chem. Int. Ed.* 60 (2021) 22722–22728.
- [46] G. Han, X. Zhang, W. Liu, Q. Zhang, Z. Wang, J. Cheng, T. Yao, L. Gu, C. Du, Y. Gao, G. Yin, Substrate strain tunes operando geometric distortion and oxygen reduction activity of CuN₂C₂ single-atom sites, *Nat. Commun.* 12 (2021) 6335.
- [47] J. Liu, Z. Wei, Z. Gong, M. Yan, Y. Hu, S. Zhao, G. Ye, H. Fei, Single-atom CoN₄ sites with elongated bonding induced by phosphorus doping for efficient H₂O₂ electrosynthesis, *Appl. Catal. B-Environ.* 324 (2023) 122267.
- [48] R. Cepitis, N. Kongi, J. Rossmeisl, V. Ivanistsev, Surface curvature effect on dual-atom site oxygen electrocatalysis, *ACS Energy Lett.* 8 (2023) 1330–1335.
- [49] G. Kresse, J. Furthmüller, Efficient iterative schemes for ab initio total-energy calculations using a plane-wave basis set, *Phys. Rev. B* 54 (1996) 11169.
- [50] P.E. Blochl, Projector augmented-wave method, *Phys. Rev. B* 50 (1994) 17953.
- [51] B. Hammer, L.B. Hansen, J.K. Nørskov, Improved adsorption energetics within density-functional theory using revised Perdew-Burke-Ernzerhof functionals, *Phys. Rev. B* 59 (1999) 7413.
- [52] J.N. Tiwari, A.M. Harzandi, M. Ha, S. Sultan, C.W. Myung, H.J. Park, D.Y. Kim, P. Thangavel, A.N. Singh, P. Sharma, S.S. Chandrasekaran, F. Salehnia, J.-W. Jang, H.S. Shin, Z. Lee, K.S. Kim, High-performance hydrogen evolution by Ru single atoms and nitrided-Ru nanoparticles implanted on N-doped graphitic sheet, *Adv. Energy Mater.* 9 (2019) 1900931.
- [53] H. Tabassum, R. Zou, A. Mahmood, Z. Liang, S. Guo, A catalyst-free synthesis of B, N co-doped graphene nanostructures with tunable dimensions as highly efficient metal free dual electrocatalysts, *J. Mater. Chem. A* 4 (2016) 16469–16475.
- [54] K. Lv, D. Wan, R. Pan, W. Suo, Y. Zhu, Curvature of NCNTs induced selectivity of CO₂ electroreduction into CO, *Carbon Neutralization* 1 (2022) 189–197.
- [55] Y. Qiao, P. Yuan, C.-W. Pao, Y. Cheng, Z. Pu, Q. Xu, S. Mu, J. Zhang, Boron-rich environment boosting ruthenium boride on B, N doped carbon outperforms platinum for hydrogen evolution reaction in a universal pH range, *Nano Energy* 75 (2020) 104881.
- [56] L. Xing, H. Gao, G. Hai, Z. Tao, J. Zhao, D. Jia, X. Chen, M. Han, S. Hong, L. Zheng, X. Huang, W. Dong, G. Wang, X. Shu, Atomically dispersed ruthenium sites on whisker-like secondary microstructure of porous carbon host toward highly efficient hydrogen evolution, *J. Mater. Chem. A* 8 (2020) 3203–3210.
- [57] Z. Yang, W. Lai, B. He, J. Wang, F. Yu, Q. Liu, M. Liu, S. Zhang, W. Ding, Z. Lin, H. Huang, Tailoring interfacial chemistry of defective carbon-supported Ru catalyst toward efficient and CO-tolerant alkaline hydrogen oxidation reaction, *Adv. Energy Mater.* 13 (2023) 2300881.
- [58] H. Zou, J. Chen, Efficient and selective approach to biomass-based amine by reductive amination of furfural using Ru catalyst, *Appl. Catal. B-Environ.* 309 (2022) 121262.
- [59] Z. Song, X. Chi, S. Dong, B. Meng, X. Yu, X. Liu, Y. Zhou, J. Wang, Carboxylated hexagonal boron nitride/graphene configuration for electrosynthesis of high-concentration neutral hydrogen peroxide, *Angew. Chem. Int. Ed.* 63 (2024) e202317267.
- [60] Z. Wang, J. Shen, S. Ji, X. Xu, S. Zuo, Z. Liu, D. Zhang, R. Hu, L. Ouyang, J. Liu, M. Zhu, B, N codoped graphitic nanotubes loaded with Co nanoparticles as superior sulfur host for advanced Li-S batteries, *Small* 16 (2020) 1906634.
- [61] L. Shi, S. Bi, Y. Qi, R. He, K. Ren, L. Zheng, J. Wang, G. Ning, J. Ye, Anchoring Mo single-atom sites on B/N codoped porous carbon nanotubes for electrochemical reduction of N₂ to NH₃, *ACS Catal.* 12 (2022) 7655–7663.
- [62] K. Guo, Z. He, S. Lu, P. Zhang, N. Li, L. Bao, Z. Yu, L. Song, X. Lu, A fullerene seeded strategy for facile construction of nitrogen-doped carbon nano-onions as robust electrocatalysts, *Adv. Funct. Mater.* 33 (2023) 2302100.
- [63] P.G. Collins, K. Bradley, M. Ishigami, A. Zettl, Extreme oxygen sensitivity of electronic properties of carbon nanotubes, *Science* 287 (2000) 1801–1804.
- [64] S. Anantharaj, S. Noda, M. Driess, P.W. Menezes, The pitfalls of using potentiodynamic polarization curves for Tafel analysis in electrocatalytic water splitting, *ACS Energy Lett.* 6 (2021) 1607–1611.
- [65] D. Cao, H. Xu, H. Li, C. Feng, J. Zeng, D. Cheng, Volcano-type relationship between oxidation states and catalytic activity of single-atom catalysts towards hydrogen evolution, *Nat. Commun.* 13 (2022) 5843.
- [66] B. Lu, L. Guo, F. Wu, Y. Peng, J.E. Lu, T.J. Smart, N. Wang, Y.Z. Finckel, D. Morris, P. Zhang, N. Li, P. Gao, Y. Ping, S. Chen, Ruthenium atomically dispersed in carbon outperforms platinum toward hydrogen evolution in alkaline media, *Nat. Commun.* 10 (2019) 631.
- [67] Q. He, Y. Zhou, H. Shou, X. Wang, P. Zhang, W. Xu, S. Qiao, C. Wu, H. Liu, D. Liu, S. Chen, R. Long, Z. Qi, X. Wu, L. Song, Synergic reaction kinetics over adjacent ruthenium sites for superb hydrogen generation in alkaline media, *Adv. Mater.* 34 (2022) 2110604.
- [68] J. Yin, Q. Fan, Y. Li, F. Cheng, P. Zhou, P. Xi, S. Sun, Ni-C-N nanosheets as catalyst for hydrogen evolution reaction, *J. Am. Chem. Soc.* 138 (2016) 14546–14549.